Version of Record: https://www.sciencedirect.com/science/article/pii/S1352231021003198
Manuscript_4231844d80bb8e4c62ec06ae0774e73b

Case study of stratospheric Intrusion above Hampton, Virginia: lidar-observation and modeling analysis

G. Gronoff

NASA Langley Research Center, Hampton, Va, USA

Science Systems and Applications Inc., Hampton, Va, USA

T. Berkoff

NASA Langley Research Center, Hampton, Va, USA

K.E. Knowland

Universities Space Research Association (USRA)/GESTAR, Columbia, Md, USA

Global Modeling and Assimilation Office, NASA GSFC, Greenbelt, Md, USA

L. Lei

NASA Langley Research Center, Hampton, Va

Universities Space Research Association, Columbia, Md, USA

M. Shook

NASA Langley Research Center, Hampton, Va, USA

B. Fabbri

NASA Langley Research Center, Hampton, Va, USA

Science Systems and Applications Inc., Hampton, Va, USA

W. Carrion

NASA Langley Research Center, Hampton, Va, USA

Science Systems and Applications Inc., Hampton, Va, USA

A.O. Langford

NOAA, Boulder, Co, USA

Abstract

*Corresponding author
Email address: guillaume.p.gronoff@nasa.gov (G. Gronoff)

On 2019-02-14, at 1:00 UTC, a large increase of ozone density at 8 km altitude was detected above Hampton, Virginia using the NASA Langley Mobile Ozone Lidar, LMOL. Ozone levels above 70 ppbv were observed down to an altitude of 4.5 km up to five hours after the start of the event. The NASA GEOS Composition Forecast (GEOS-CF) model was used to investigate the hypothesis of a stratospheric intrusion (SI). The agreement between the model and the observations confirmed the stratospheric origin of the airmass and highlighted the capabilities of GEOS-CF to simulate intrusions. In parallel, MicroPulse Lidar (MPL) observations indicated that depolarizing particulates high in the troposphere showed downward motions linked to the intrusion. Since these particulates are linked to cirrus clouds, it is hypothesised that the SI led to an ice-virga effect. This might suggest that particulate observations can exhibit patterns of stratospheric intrusions and can be used, in certain cases, as a signature of the events. These particulates, likely ice crystals, have opposite distribution gradients compared to O_3 at their interface which could be explained by a non-mixing of stratospheric and tropospheric air-masses as well as destruction of O_3 by ice crystal-induced processes. Model-data comparison shows that if that latter effect exists, it has small consequences for the observed case. This work shows the capabilities of the LMOL system to detect SI and to validate the vertical and temporal modeling of SI by GEOS-CF, as well as showing that signatures of SI could be detected by MPL.

Keywords: Lidar, Ozone, Stratospheric Intrusion, Model

2010 MSC: 00-01, 99-00

---

1. Introduction

Stratospheric intrusions, SI, are the injection of stratospheric air masses into the troposphere typically leading to an increase of ozone (O_3) density [1, 2, 3]; such increases can directly or indirectly impact the ground-level O_3 concentrations and affect local air quality (AQ) [4, 5, 6].

SI events are frequent near the jet streams (far more frequently near the

polar front jet than the subtropical jet) [7], as the tropopause is drawn down wrapped around the jet core, known as a "tropopause fold" [8]. Spatially, SIs are about 100-300 km wide in the crosswind direction and several hundreds of kilometers long [9]. Since SIs are mesoscale fine-scale features, they are best identified in model and reanalysis products with horizontal resolutions of 50 km or finer [10, 11, 12, 13, 14]. The model-data comparison (see, e.g. [15, 7]) shows that, for 2-hour windows, over the whole year, the frequency of tropopause fold event is 12% in the Northern Hemisphere and 9% in the Southern Hemisphere. The area covered is 13% and 11% for the Northern and Southern Hemispheres, respectively.

The addition of stratospheric O_3-rich air in a moderately polluted environment, or the direct transport to communities at high elevation, can lead to an exceedance of the US National Ambient Air Quality Standard (NAAQS; maximum daily 8-hour average $O_3 > 70$ ppbv [16]), and therefore have negative health effects to humans and vegetation as demonstrated in Langford et al., 2009 [17]. In order to accurately forecast surface O_3 air quality, it is critical these models can accurately represent SI events. Due to their dynamic nature, SIs are accurately modeled on their spatial scales, but their transport down to the ground could be complicated by local meteorology, topography, and other sub-grid scale processes [11, 18].

Validation of SI representations in models are traditionally done using local observations, such as spectrophotometers to get the spatial extent (e.g., PANDORA [19]) or satellite data [13]. Other techniques could involve airborne in-situ observations [1, 12, 18]; water vapor observation by lidar [20]; limb sounding [21, 14]. One need for the validation of SI models lies with the vertical distribution of tropospheric O_3. Ozonesondes can be used for that purpose. The lidars from the Tropospheric O_3 Lidar Network (TOLNet), a joint effort of NASA, NOAA, and ECCC, are especially well adapted for these later studies [e.g., 18] since they are able to retrieve vertical profiles several times per hour.

In this paper, we investigate the comparison of an O_3-lidar and a Micro-Pulse Lidar (MPL) observations which exhibited stratospheric O_3 concentra-

tions on 2019-02-13 and 2019-02-14 with NASA's GEOS Composition Forecasting (GEOS-CF) system, a combined chemistry and meteorology model running in near-real time. Generally, springtime is the season when SIs have the largest impact on surface O_3: while tropopause folds occur year round [see e.g. 15], during the winter and early spring there is a build-up of O_3 in the lower stratosphere [22] which is being drawn upon in the SI. In addition, we highlight the effects of the SI on the particulate dynamic over the region and suggest the use of MPL (or a ceilometer) to help validate models if no O_3 lidars are present. In Section 2, we describe the instruments and model used. In Section 3, we present the synoptic-scale weather conditions and the observations of the SI of 2019-02-14 above Hampton, Va, USA, before presenting the comparison with modeling in Section 4. We discuss the interaction between O_3 from the SI and the particulates in Section 5. A final summary is given in Section 6.

2. Data

2.1. LMOL: the Langley Mobile Ozone Lidar

The Langley Mobile O_3 Lidar, "LMOL", is a TOLNet lidar dedicated to the study of tropospheric O_3, based at NASA Langley Research Center in Hampton, Virginia, USA, (37.0954 °N, 76.389 °W) [23]. It is a highly mobile lidar that has been used in several NASA campaigns such as OWLETS I and II, LISTOS [24, 25, 26], and SCOOP [27]. Its current configuration, close to the one presented in Gronoff et al. (2019) and Farris et al. (2019) [28, 29], is able to retrieve a maximum profile from 100 m to 10 km altitude at night, under clear sky conditions. During daytime, the maximum altitudes are lower, typically 5 km, due to the contamination by the scattered solar ultra-violet. TOLNet dictates rules for the acquisition, processing, and archiving of the data that assure the quality and consistency of the products. TOLNet defined a best practice for vertical resolution computation [30], cross sections uses, and uncertainty calculations [31] as followed by the LMOL retrieval algorithm [27]. LMOL is in a DIAL (DIfferential Absorption Lidar) configuration for retrieving O_3, i.e. two

lidar channels are used, one significantly more absorbed by O_3 –the on-line– than the other one –the off-line– allowing to mathematically infer the O_3 density from the differences in the signals. For the current work, the tunable laser, based on a Ce:LiCAF crystal [23], was used with an online (high O_3 absorption) wavelength of 286.6 nm and an offline (low O_3 absorption) of 292 nm (in the Hartley band). The vertical resolution, varying from 100 m at 1 km altitude to 2 km at 10 km altitude at night was optimized to yield a O_3 density uncertainty of 10% for profiles averaging the data acquired during 5 minutes. At a constant time averaging, improving the (non-systematic) uncertainty is indeed done by averaging data over a larger range of altitudes, therefore decreasing the resolution [28].

For the comparison with the model, the time averaging was increased from 5 minutes to 1 hour, centered at the hour, since the model provides a snapshot of the atmosphere on the hour; the 10% uncertainty was kept while smoothing, allowing improvements of the vertical resolution.

2.2. MPL: the Micro-Pulse Lidar

The NASA Langley Micro-Pulse Lidar, "MPL", is a 532 nm lidar co-located with shortwave radiometers at the CERES Radiation and Validation Experiment -Langley Research center site located on a marsh/grass area at NASA Langley Research center, 200 m from LMOL. (The Chemistry And Physics Atmospheric Boundary Layer Experiment –CAPABLE– and the Virginia Department of Air Quality site are also located there). It is part of the micro-pulse lidar network, MPLNET [32], dedicated to the observations and characterization of particulates, clouds, and boundary layer height. The instrument used has a depolarization channel which allows the characterization of the asphericity of the observed particulates (which is linked to their type, e.g. dust, smoke, clouds, etc.; in the current case to help point to an ice composition [33]). The MPL used for this study is based on a Nd:YVO4 laser, repetitively pulsed, at 1064 nm doubled at 532 nm. The laser beam is then polarization controlled using a ferroelectric liquid crystal. Then the pulses are sent to the atmosphere and are

retrieved using the instrumentation as described in Flynn et al. 2007 [34]. The data processing is done by the MPL-NET group (https://mplnet.gsfc.nasa.gov/) led by Dr. Ellsworth Judd Welton. Data is transferred once an hour via a script from the MPL data collection laptop at NASA LaRC to the MPL-NET database. The calibration of the MPL is performed once a month .

2.3. The GEOS Composition Forecast System

The NASA GEOS high-resolution model and data assimilation products are publicly-available, high global resolution datasets trusted in the analysis of SI both by atmospheric dynamics and for the representation of stratospheric O_3 [12, 13]. GEOS-Chem, a chemistry module, has been used along with the meteorology provided by GEOS to study the transport of ozone in local and global pollution events in collaboration with TOLNET Lidars [26, 35]).

NASA's GEOS-CF system is a near-real time product from NASA's Global Modeling and Assimilation Office, which provides realistic estimates of stratospheric and tropospheric chemical concentrations, with meteorology, stratospheric O_3, and fire emissions constrained by observations [36]. The GEOS-CF system first runs a meteorological "replay" [37] for the past 24-hours in order to have the best initial conditions prior to running the 5-day forecast. During the replay segment, the GEOS atmospheric general circulation model is constrained to the analyzed meteorological and aerosol fields from GEOS Forward Processing for Instrument Teams (GEOS FP-IT; [38]) while one-way coupled to the GEOS-Chem version 12.0.1 chemistry module [39, 40, 41, 42] with full tropospheric and stratospheric chemistry [43]. In addition, the GEOS-CF weakly nudges the stratospheric O_3 towards the numerical weather prediction GEOS Forward Processing (GEOS-FP) system's 3-hourly average assimilated O_3 product which is constrained by satellite observations of O_3 (mainly the Microwave Limb Sounder and the Ozone Monitoring Instrument onboard Aura [see e.g. 44], and since March 2019 the Ozone Mapping and Profiler Suite Nadir Mapper [see e.g. 45]).

Since each 24-hour replay is used to start the next day's replay simulation,

the replay segments can be used together as a continuous dataset for analysis of the meteorology and chemistry on the same high spatiotemporal resolution: global horizontal resolution is 0.25°, nominally 25 km, on 72 model layers from the surface to 0.01 hPa; and "surface" fields (the lowest model layer, approximately 130 m thick) are saved every 15-minutes and all other 2-dimensional (2-D) and 3-D fields are saved every hour (For full details on emission inventories and model set-up see Knowland et al., 2020 [46]).

Similar to other GEOS data assimilation products, the GEOS-CF can be used for analysis of SI events since it is a high resolution global model with realistic stratospheric O_3. Here, we use the 3-D O_3, vertical velocity (ω), Ertel's potential vorticity (PV), and equivalent potential temperature (θ_e) interpolated to 24 geopotential height (GPH) levels from 0 to 18 km and the 3-D PV, GPH and potential temperature (θ) on 23 pressure levels from 1000 to 10 hPa. In addition, we use the 2-D sea level pressure (SLP) and 2 m temperature diagnostic (T2m).

3. The 2019-02-14 SI Observations

3.1. Observation by LMOL

In Figure 1 we show the curtain obtained from 2019-02-13 18:00 UTC to 2019-02-14 20:00 UTC. It is local nighttime from 2019-02-13 22:00 UTC to 2019-02-14 12:00 UTC, so the maximum altitude is affected mainly by the presence of high-altitude clouds or large O_3 absorption. After 12:00 UTC, the solar contribution lowers the maximum altitude down to 5 km.

The signature of the SI is seen from 2019-02-13 21:00 UTC to 2019-02-14 03:00 UTC with O_3 values above 100 ppbv between 10 and 6 km altitude. After 2019-02-14 04:00 UTC, the values in the 6 to 8 km altitude ranges are in the more usual range of 40 to 60 ppbv. After 2:00 UTC, we observe a tongue of high O_3, with values around 80 ppbv, with relatively cleaner air ($O_3 < 60$ ppbv) above and below. The mean altitude of this tongue goes from 5.5 km at 02:30 UTC to 4.5 km between 05:00 UTC and its disappearance at

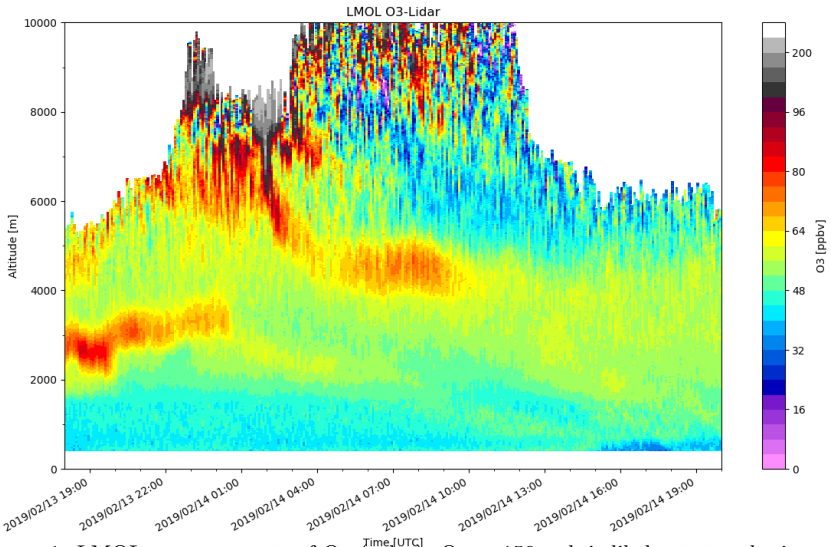

Figure 1: LMOL measurements of O_3 (color). $O_3 > 150$ ppb is likely stratospheric.

10:00 UTC. It is important to note that these high values of O_3 are not affected by particulates contamination (see [47] on how aerosols modify O_3 measurements from DIAL), as shown in Section 3.2 (see also Figure 2), and therefore are not an algorithmic bias (we applied an aerosol correction to our observations and found no differences with no corrections). Finally, we observe the remnants of another possible SI at 3 km altitude on 2019-02-13 18:00 UTC and thereafter.

The intrusion of stratospheric O_3 cannot be entirely demonstrated by such a curtain since SI are typically 3-D events: the downward motion is accompanied by a horizontal motion. Therefore, even if it would be tempting to consider that the pocket of O_3 observed at 7:00 UTC at 4.5 km altitude is connected to high O_3 mixing ratio reaching down at 02:00 UTC at 7 km altitude, it might be erroneous since they are possibly not from the same airmass when horizontal wind is present. The modeling by GEOS-CF can help validate that the downward motion and the pocket are linked to the same event (see also Section 4).

3.2. Observation by the MPL and comparison with LMOL

The MPL data (Figure 2, top) were initially investigated to check to see if cirrus clouds were observed (MPL depolarization > 0.1) near the time the event was observed. These data indicate that clouds existed only above the high O_3 values (Figure 1), therefore showing that the tongue of high O_3 descending into the troposphere was not an artefact.

A closer inspection of the depolarization channel shows particulates (depolarization at 0.05) descending into the troposphere similar to the SI, likely along the same isentropes (Figure 3, Panel 3) from around 2:00 UTC then staying aloft. However, these particulates, apparently linked to the cloud at 7 km altitude

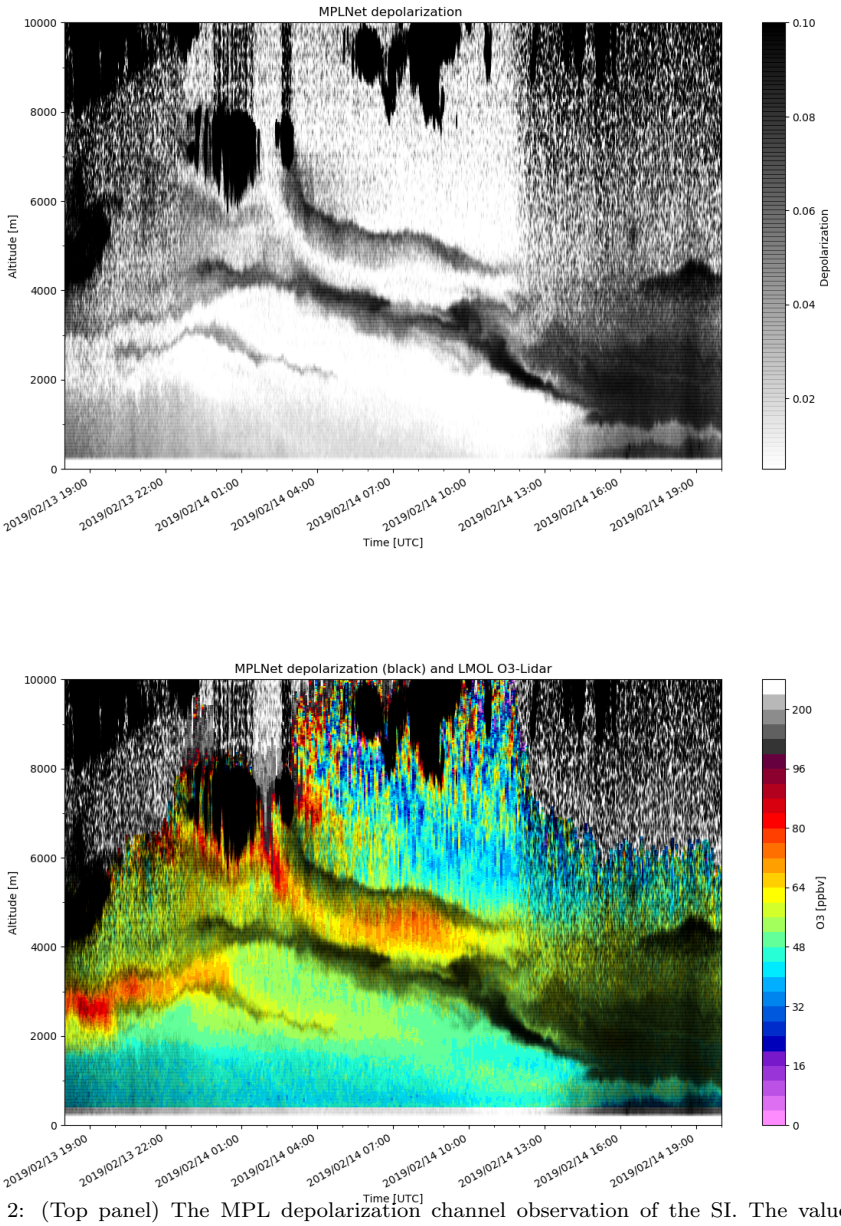

Figure 2: (Top panel) The MPL depolarization channel observation of the SI. The value reported are the volume depolarization ratio (ranging from 0 to 1). (Bottom panel) Overlap of the MPL depolarization channel (black and white) over the LMOL data

(near the tropopause) observed at 2:30 UTC, seem to be at a higher altitude than the O_3 pocket, and there seems to be another layer at lower altitude.

A precise comparison of the location of these particulates with respect to the high-O_3 values (Figure 2, lower panel, overlapping Figure 1) shows the onset of the the SI. The interesting finding is that the particulates do not enter the stratospheric air, but merely surround it; this is valid for both the event at 02:00 UTC on 2019-02-14 and the following O_3 pocket, but also for the high O_3 values on 2019-02-13 at 2 km altitude. In addition, most of these particulates seem to be falling from the cirrus clouds that appear in the data before and after the intrusion in itself. It is worth noting this occurs even though the amount of depolarization linked to the cloud at 01:00 UTC is way smaller than the one linked to the 02:00 UTC cloud and that this depolarization is not a bias due to the processing of the MPL data linked to an O_3 absorption: if it were the case, the particulate layer at 2 km altitude between 0:00 UTC and 4:00 UTC, linked to a minute increase of O_3, would not be that strong; the same could be said for the layer at 4 km altitude between 22:00 UTC (on the 13th) and 03:00 UTC.

The dynamical nature of this event and of these particulates will be discussed in detail in Section 5. It can however be observed that the depolarization channel is, in the present case, highlighting the interface between air masses, and has therefore a signature of the SI.

3.3. Meteorology

Favorable synoptic conditions for a SI are linked to the cyclonic activity, as described in [48, 49]. Focusing on 2019-02-14 02:00 UTC, the time when we observed the high concentration of O_3 (> 70 PPBV) at less than 8 km altitude, the synoptic situation leading to the SI over the LMOL site was dominated by a broad area of cyclonic activity covering the northeastern US and southeastern Canada, as well as a surface high pressure area over the southeast US (Figure 3, a). GEOS-CF data on 2019-02-14 01:00 UTC indicates that the cyclonic region consisted of two separate surface lows: a decaying low located in southwestern Quebec, and a strengthening low near Nova Scotia (Figure 3, a). A cold front

attached to the strengthening low crossed over LMOL around 2019-02-13 03:00 UTC (not shown) and subsequently moved offshore into the western North Atlantic Ocean; a line of clouds along and behind the surface cold front is clearly visible in infrared satellite imagery (not shown).

Higher in the atmosphere, the cyclonic system had substantial support from a deep upper-level system centered near southwestern Quebec; the GEOS-CF data show this system had closed circulation up to the 300 hPa level (Figure 3, b), and an upwind trough axis persisted all the way up to 100 hPa (not shown). The meridional extent of this trough was also significant, stretching from Ontario to the Gulf of Mexico (Figure 3, b). A polar jet with a wind speed maximum ($>$ 170 kts) located near 250 hPa (Figure 3, c) was situated behind and parallel to the surface cold front and ahead of the trough axis (just offshore of the US East Coast at 01:00 UTC). Tropopause folds that can transport air from the stratosphere into the troposphere are known to form in the vicinity of the polar jet [50].

This behavior can be seen in Figure 3, c, the cross-section of wind speed and tropopause height (here defined as the level at which potential vorticity reaches 2 PV units, 1 PVU = $10^{-6}2\ \mathrm{s}^{-1}\ \mathrm{K\ kg}^{-1}$) passing over the LMOL site. Throughout the day on 2019-02-13, wind speed steadily increases above 400 hPa, reaching a maximum of over 170 knots at 250 hPa around 21:00 UTC. Immediately after the passage of the jet maximum, the tropopause height decreases from around 230 hPa to 410 hPa on 2019-02-14 01:00 UTC. Further, the descending isentropes from that point onward at 400 hPa and below would support isentropic transport from the tropopause fold lower into the troposphere. In the next sections, the meteorological and chemical conditions of the atmosphere, during the time of the likely SI observed by LMOL, are investigated using the GEOS-CF replay data.

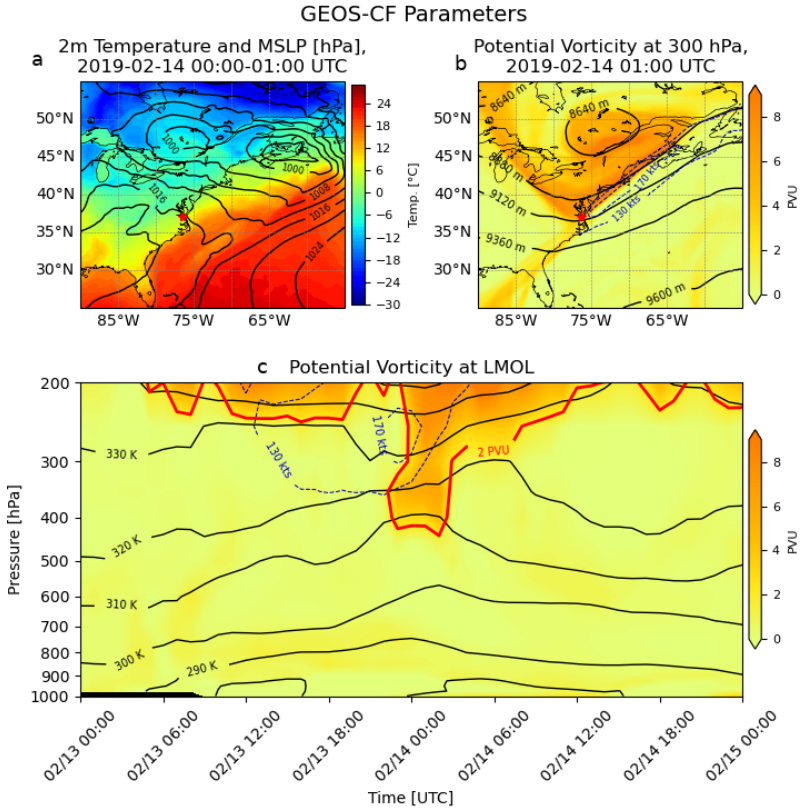

Figure 3: Panel a (top left):SLP (black contours) and T2m (shading) from GEOS-CF at 01 UTC on 2019-02-14. The location of the LMOL site is indicated by the red star. The two separate cyclones are visible here, as is the temperature gradient representing the surface cold front stretching from the eastern cyclone southwestward to near the coast of the southeast US. Panel b (top right): GEOS-CF 300 hPa PV (shading; 1 PV unit (PVU) = 10^{-6} m^2 s^{-1} K kg^{-1}) and GPH (solid black lines) at 01 UTC on 2019-02-14. Also shown are isotachs starting at 130 kts (dashed red lines). The location of the LMOL site is indicated by the red star. The polar jet is clearly visible, with a maximum on the leading edge of the trough. Panel c (bottom): Curtain plot of PV at the GEOS-CF grid point closest to the LMOL site (37°N, 76.5^{o}W) from 2019-02-13 to 2019-02-15 UTC. The approximate height of the tropopause is indicated as the 2 PVU contour (red line; 2 PVU values below 800 hPa are ignored, as these are due to diabatic heating or frictional effects). Also shown are isentropes (θ; solid black contours) and isotachs as in Panel b (dashed brown lines).

4. Modeling of the Stratospheric Intrusion

The GEOS-CF model simulated the SI event over NASA Langley on February 13-14, 2019 both in the synoptic meteorology conditions (Figure 3) but also in the O_3 concentrations (Figure 4) similar to the observed O_3 curtain by LMOL (Figure 1). The location for this curtain is the GEOS-CF grid box closest to LMOL, with the GEOS-CF data interpolated to constant GPH levels at a vertical resolution of 500 m up to 9 km and then 1 km up to 12 km. The time resolution is 1 hour.

On 2019-02-13, 18:00 to 22:00 UTC, prior to the tropopause folding event on February 14th occurring over LMOL, there are two filaments of enhanced O_3: 7-8.5 km and 2.5-3 km (Figures 1 and 4). Both are from isentropic descent of O_3 to the southeast from the tropopause fold, remaining behind the front (Figure 5). As the depressed tropopause passes over LMOL (2 PVU contour below 7 km 2019-02-13 22:00 UTC through 2019-02-14 01:00 UTC; Figures 3, c and 4), there is a sharp increase in O_3 concentrations in the 7-8.5 km layer (between 80 and 150 ppbv; Figure 4), with descent – indicated by negative ω – of O_3-rich air (> 60 ppbv) isentropically to 5 km in the first hours of 2019-02-14 with the tongue of $O_3 > 52$ ppbv around 4 km altitude lasting until 09 UTC. As the front continues eastward, the tropopause fold moves northward, leaving elevated levels of O_3 in the lower troposphere and continued descent of O_3-rich air (Figures 4 and 5).

This agreement between the model and the observations, with the 3-D synoptic set-up, supports the hypothesis that the LMOL observed a SI. However, there are a couple of notable differences between the model and the observation which are mainly linked to the pocket of O_3: in the observations, the layer is about 1 km higher than in the modeling and has higher levels of O_3, on the order of 80 ppbv to be compared to the 50-60 ppbv in the model. On the other hand, the modeled layer is thicker than the observed layer (a little less than 2 km to be compared with 1 km, both model and observation having a better than 500 m resolution). This means that the amount of O_3 inside the layer is

comparable between model and observations.

In Section 5, we will look in more details at the comparisons between the different instruments and the modeling.

5. Discussion

5.1. Model-data comparison of O_3

In Sections 3.3 and 4, the GEOS-CF model simulated, by both dynamics and O_3 concentrations, a SI event over Hampton, Virginia, that was observed by LMOL.

GEOS-CF provides a snapshot of the 3-D atmosphere every hour, therefore the LMOL data were re-processed with the same time resolution. This notably led to a 200 m vertical resolution in the 4 to 6 km altitude layer during the night (because more integration time leads to better signal-to-noise and therefore requires less vertical integration). In Figure 6 we show the averaged difference between the model and the observations between 2019-02-13 18:00 UTC and 2019-02-14 18:00 UTC. It is to be noted that the LMOL data with more than 15% uncertainty were filtered out in that comparison and that the bins affected by clouds were filtered out as well.

Overall, the bias between the observation and the model has an average of 2.9 ppbv; this is within the uncertainty of the observation. The standard deviation is 16.6 ppbv; this highlights the variability of the event (which is difficult to perfectly compare within the model-data comparison since the timings can be off and since the model resolution is 1 hour). Even if the model under-represented the peak amount of O_3 in the 5 km layer pocket (Figure 7), it predicted the whole dynamic of the event, and therefore does not fundamentally require more parameters to fully comprehend the O_3 data.

The top row in the Figure 7 shows the onset of the SI as observed by LMOL and modeled by GEOS-CF. In these panels, the maximum altitude of LMOL is limited by the presence of cirrus clouds, as seen in the MPL data. It can be seen, above 6 km altitude, that LMOL is retrieving the O_3 enhancement as

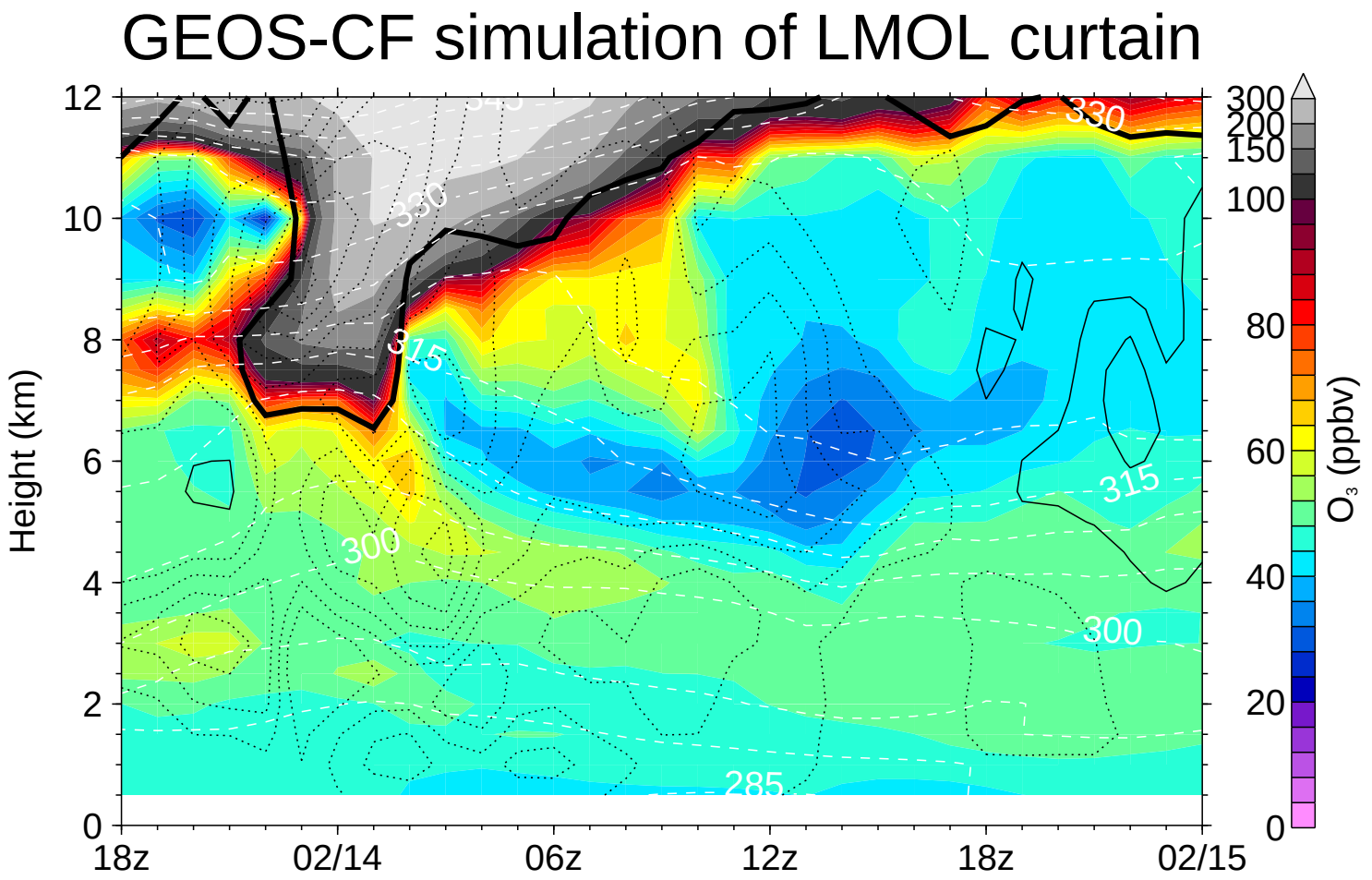

Figure 4: Curtain plot of GEOS-CF O_3 (color), θ_e (dashed white contours; 5 K intervals), ω (dotted for descent, thin solid black for ascent) and the dynamical tropopause (thick black line; 2 PVU) for the grid-box including LMOL for the period from 2019-02-13 18:00 UTC to 2019-02-17 00:00 UTC.

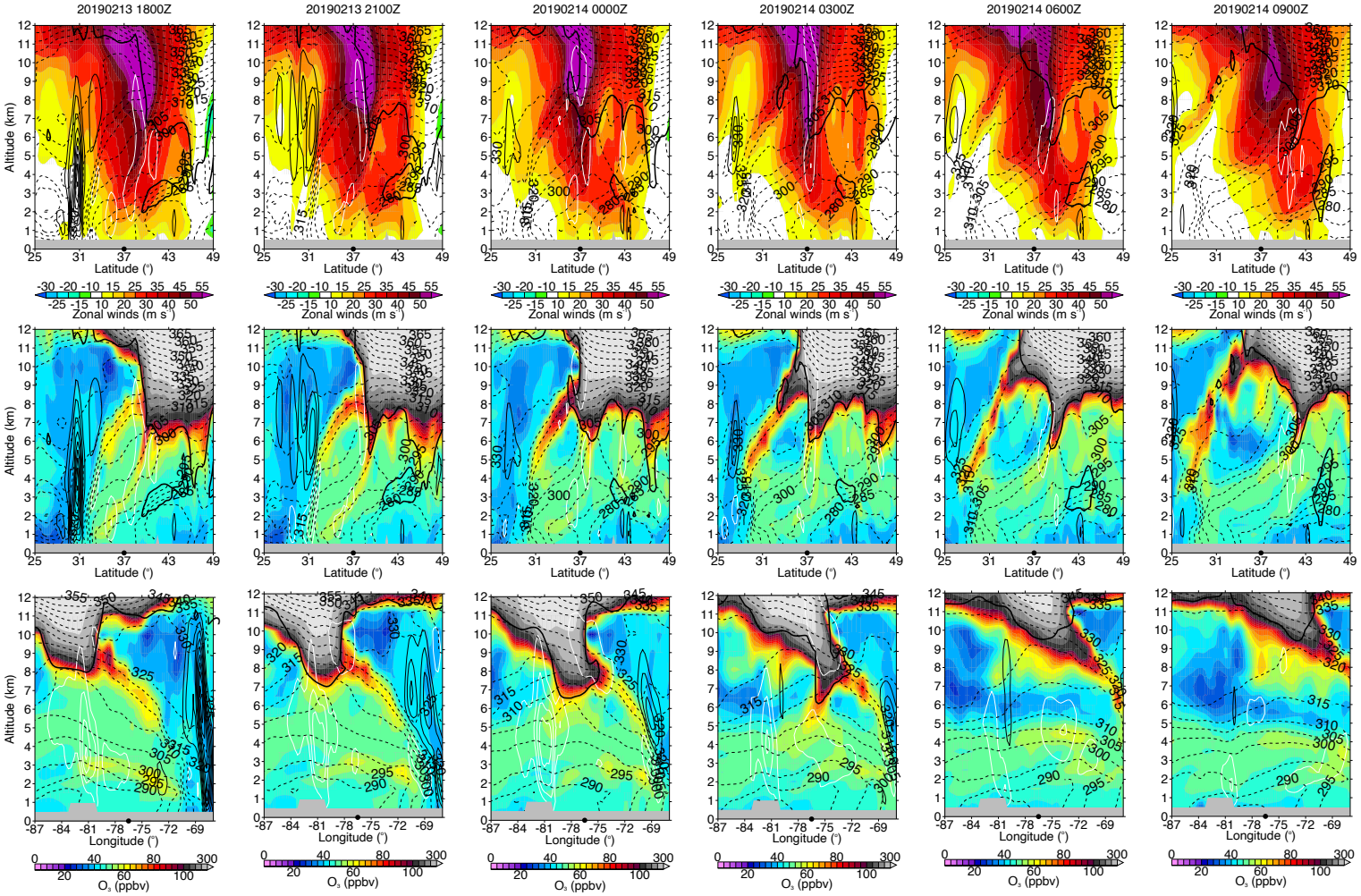

Figure 5: Vertical transects North-South (top and middle rows) and East-West (bottom row) of the zonal winds (color; top row) and O_3 (color; middle and bottom rows) from the GEOS-CF centered on the location of LMOL (black dot on x-axis) every 3 hours from 2019-02-13 18:00 UTC to 2019-02-14 09:00 UTC. Also in each plot are θ_e (dashed lines; 5 K intervals), ω (white contours for descent, thin solid black for ascent) and the dynamical tropopause (thick black line; 2 PVU), similar to Figure 4.

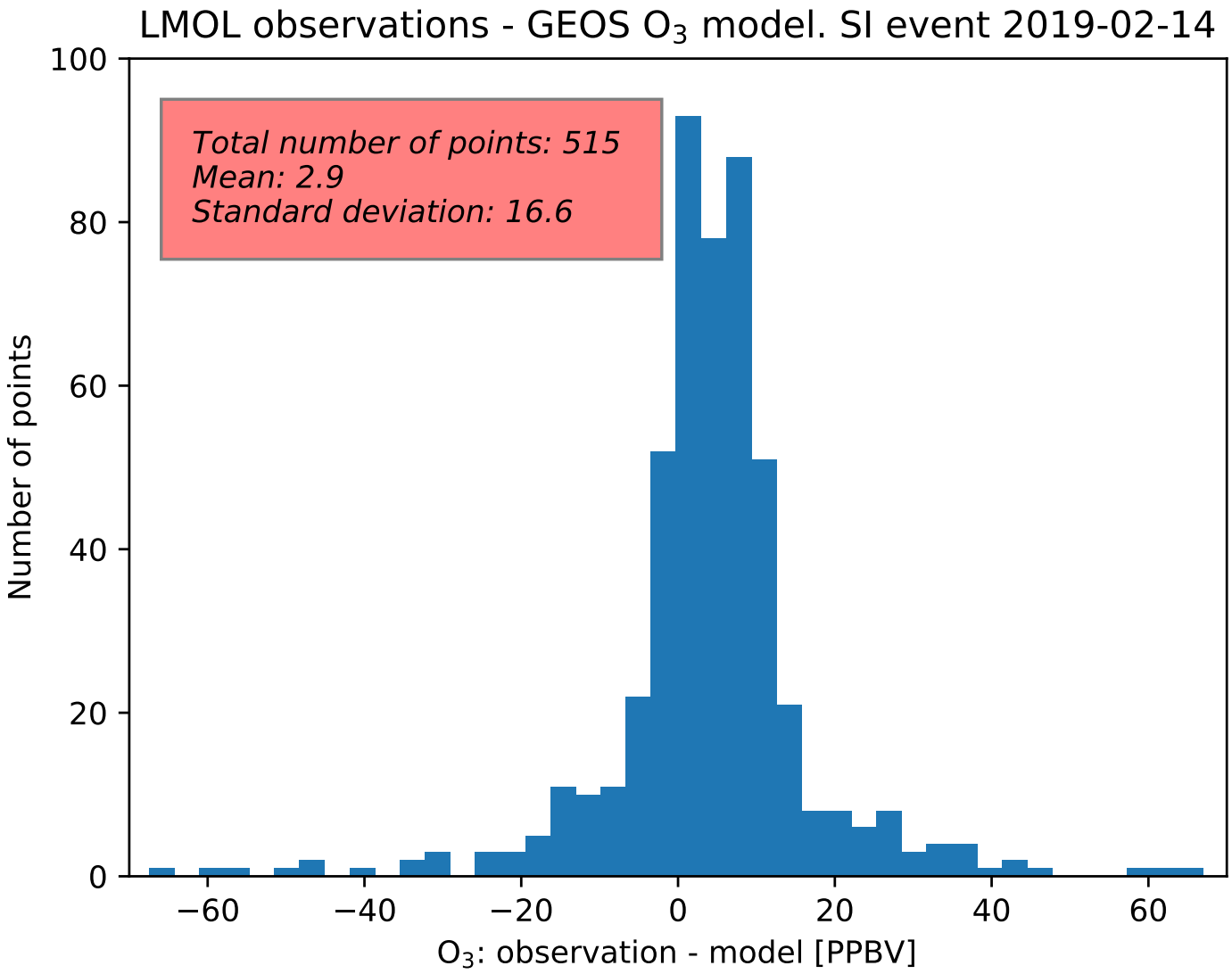

Figure 6: Statistical comparison of GEOS and LMOL

predicted by the model. The observations show slightly more O_3 at 6 km, this small bump corresponds to the enhanced values that are linked with the low altitude intrusion. The small differences at 7 km altitude between the model and the observations, on that first row, can be explained by the large gradient of O_3, which is both difficult to model accurately and may be slightly biased in the retrieval (since it is in the upper range of the lidar and has vertical resolution on the order of 500 m). The model seems however to be under-predicting the onset at 02:00 UTC and over-predicting at 04:00 and 05:00 UTC (at around 8 km altitude). If there were no cirrus clouds, we would have expected to see intrusion of O_3-rich air without any new particulate falling down (highlighted by the depolarization channel in the MPL data); in addition, the air descending from the stratosphere would have been rich in O_3. In the present case, it is possible that the cirrus clouds have an impact on O_3, explaining why LMOL observes less O_3 than predicted when the air-masses have been affected by the clouds, like one hour after the intrusion, at 3:00, as shown in the MPL data (Figure 2). In that case, the particulates distribution tends to indicate a downward motion, if that air is coming from the stratosphere, it means that it has been depleted in O_3; another interpretation of that observation, discussed in details in the following, is that the particulate-rich airmasses are tropospheric, and they are just displaced by the folding. It is also to be noted that the time resolution of one hour renders the comparison difficult since the 5-min LMOL observations shows a very fast intrusion of O_3: at 6 km altitude, the O_3 values is above 80 ppbv for a duration between a half-hour to an hour. Below 6 km altitude, for the whole panel of Figure 7, the model and the data agree correctly except at the location of the pockets of O_3 that are linked with SI. In these pockets, the O_3 densities are observed to be higher than in the model. These pockets are also observed to be surrounded by high-depolarization regions. The pockets of O_3 are not expected to be homogeneous, however, it should be noted that their gradient is anti-correlated with the depolarization gradient at their interfaces.

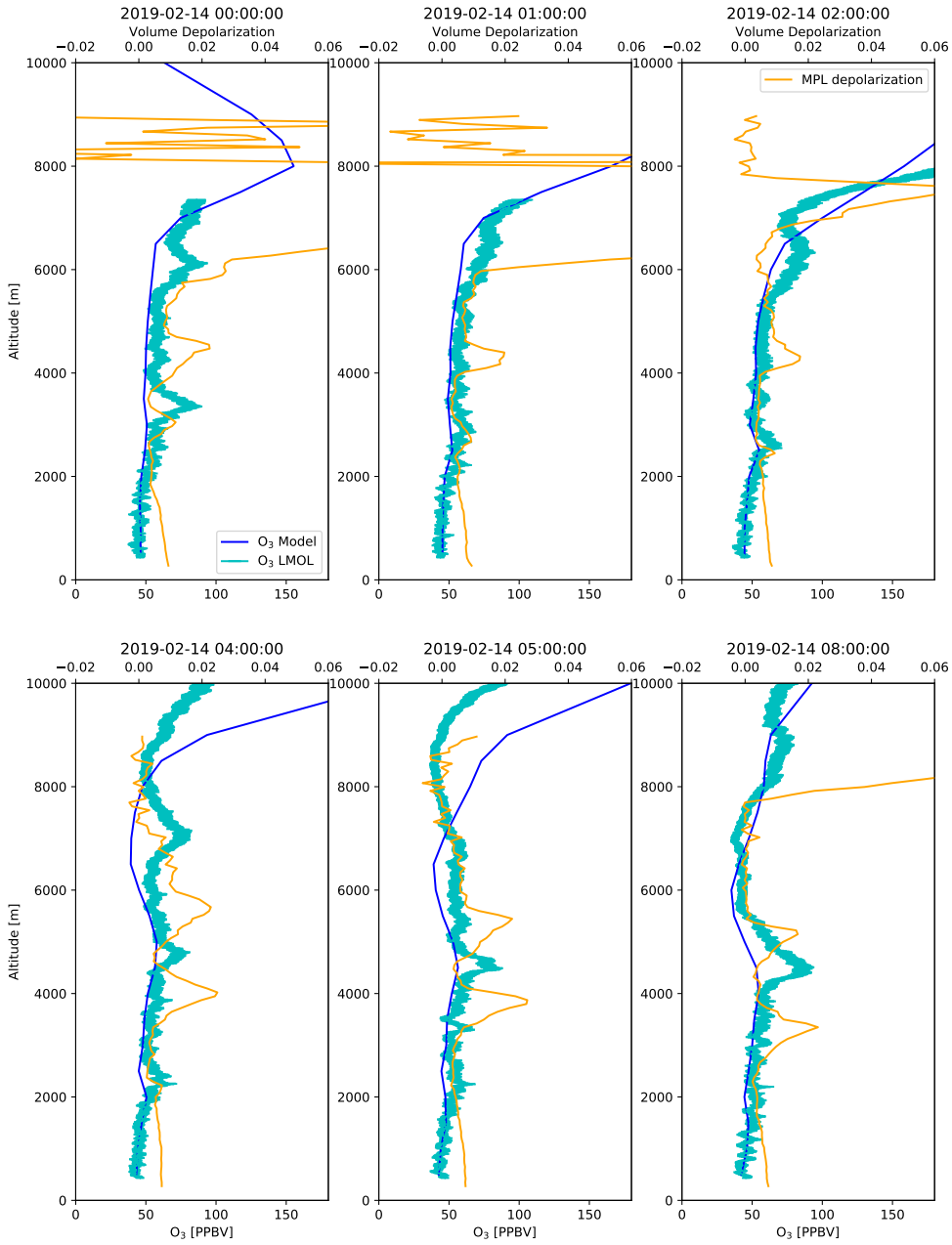

Figure 7: Comparison of the volume depolarization channel with the O_3 values from LMOL and GEOS-CF for specific vertical profiles. The excellent comparison between the model and LMOL can be found at all altitudes that are not impacted by the cirrus clouds. At 8:00 UTC, it is easily found that the O_3 layer is surrounded by depolarizing particulates.

5.2. What happened in the depolarization channel?

Figure 2 (lower panel) shows the surprising relation between the particulates as observed by the MPL depolarization channel and the O_3 as observed by LMOL: it was not expected to see an O_3 layer sandwiched between particulate layers. Indeed, past SI have shown particulates coming along with the O_3 [3] and the upper troposphere was mainly depleted of particulates an hour before the SI. Since these particulates are depolarizing and are linked to downward winds coming from cirrus clouds, it is likely that they are ice crystals: in rare cases, spherical particules can be formed in cirrus clouds, but it requires peculiar conditions as explained in [51].

First, it is to be noted that the interaction between the ice crystals and O_3 is not an artifact of either lidar: the analysis of the backscatter ratio from LMOL using the offline wavelength implies that the uncertainty in O_3 due to particulate contamination is well below the uncertainty of the retrieval due to the other sources (cross sections, temperature and pressure profiles used for the retrieval, etc.). Conversely, O_3 does not affect the MPL return, otherwise the volume depolarization ratio would follow O_3 behavior in every location, and would be extremely visible at, e.g, 2000 m altitude on 2019-02-13 19:00 UTC, just below the high O_3 spot.

Second, the particulate layer above the high-O_3 has a direct link to the cirrus cloud at 03 h UTC. This is very likely due to the downward winds due to the SI, bringing ice crystals from the cirrus down. If it is the case, there must be a process depleting the O_3 from that descending air. The other possibility is that it is a different air-mass and the difference in temperature creates ice layers at the interface as in [52]. We used the GEOS-CF model to check if this could be the case. The temperature of the air at 7 km altitude at the onset of the SI is about -40^{o}C, and the temperature of the surrounding air is about -20^{o}C or lower. In the time-span studied here, the temperature above 4 km altitude, is -15^{o}C or lower; the temperatures become positive below 2-3 km altitude. Processes of surpercooling, as described in [33], could lead to the cold airmass making ice crystals at the interface, however, it seems less realistic

due to the temperature being lower than -37^{o}C above 8 km altitude. This is a very different event than what was observed previously such as in the work of Browell et al. 1987 [3]: instead of having the particulate layer within the the SI, it is surrounding it, meaning that different physical or chemical processes are involved. It is, however, similar to the observations of Reichardt et al. 1996 [53] that presented low values of O_3 near cirrus clouds. The work of Roumeau et al. 2000 [54] suggests that O_3 is depleted when interacting with ice crystals. Such an interaction is compatible with the observations of O_3 and ice crystals between 2:00 and 3:00 UTC on 2019-02-14: after the intrusion, in the 6 to 8 km range, when cirrus clouds or ice crystals are present in the airmass, the O_3 is depleted contrarily to when they are not present. The vertical distribution of these ice crystals is compatible with the interpretation of a downward motion of an O_3-rich airmass initially coming from the stratosphere that was depleted by its interaction with the ice crystals. This observation is not incompatible with a non-mixing between the SI airmass and a ice crystal-rich airmass, but makes the strong build-up of ice crystals after the intrusion more difficult to explain. In [54], the mechanism for depletion is theorized to be an increase in O_3 interaction with active chlorine compounds. These chlorine compound having been activated by hetereogenous reactions at the surface of the ice crystals [55]. Since the density of these compounds decreased since 1999 [56, and references therein] the ice crystal depletion effect should not be as efficient; however, it is to be noted that the magnitude of the depletion was higher than expected in 1999. If the depletion of O_3 through interaction with ice crystal (direct or indirect –like the chlorine pathway–) is found to be significant, a different chemical destruction pathway remains to be found, which is compatible with the conclusion of Reichardt et al. 1996 [53]. Such a mechanism was proposed in Meier et al. 2002 [57] where it was theorized that up to 14% of O_3 could be destroyed on the surface of ice crystals through the interaction with nitric acid (HNO_3). Another interpretation would be that the intrusion is layered between ice crystals-rich air masses, and that the 3D dynamics of the SI leads to the layering. This could explain the apparition of the particulate layer under

the O_3 layer on 2019-02-13 20:00 UTC. This is the interpretation of Jacob 2000 [58] of the [53] results; however, Wang & Sassen, 2000 [59] show that this interpretation is valid for low altitude clouds and that depletion happens in high altitude clouds, an observation that was confirmed later [60]. An interesting hypothesis is the possibility that the observed particulates are actually seeding the cirrus cloud as observed in other settings [61]. In that case, the O_3 rich layer would have been in between particulate-rich layers before the intrusion. In such a case, stratospheric particulatess are linked with the depletion of O_3 as described in [62], it is however less likely here since the particulates are not observed independently of the cirrus.

Overall, it seems likely that both kinds of interaction – ice crystal depletion and SI in between two crystal-rich air layers – are playing in the event of 2019-02-14, since the downward air motion linked to a SI is known to enable the formation of the cirrus clouds from where the ice crystals can be extracted. Our observations do not allow to quantify the importance of each processe and therefore to conclude on the dynamics and depletion strength. Further work on the interaction of SI and cirrus clouds as well as on the interaction of O_3 with ice crystals is necessary to conclude on the importance of each process in the observed event.

6. Conclusion

A SI event over the United States was observed on 2019-02-14 by LMOL and confirmed with the modeling by GEOS-CF. Over this event, the observation and the model had an average bias of 2.9 ppbv and standard deviation of 16.6 ppbv. The event led to an aloft layer of O_3 surrounded by ice crystals layers observed by the NASA LaRC MPL. The link between the ice crystals and the cirrus clouds present after the SI led to a signature of the SI in the depolarisation channel of the MPL.

This is the first time a SI has been observed indirectly with a MPL along with a direct observation by an O_3 lidar. If the conditions that lead to the presence

of depolarization around the SI are better understood, we could use the MPL to detect SI through their signature in this channel. This would increase the amount of instruments able to detect SI since there are fewer O_3 tropospheric lidars than MPLs. The exact nature of the interactions between the ice crystals and the O_3 from the intrusion remains however to be explained in detail; the observation suggests that O_3 depletion by the ice crystals and non-mixing of air-masses are important processes. It is also likely that the cold air from the intrusion (as confirmed by GEOS-CF) helps the formation of the crystals at its boundary with more humid air, which in turn destroy the O_3 diffusing out of that interface, leading to a strongly determined O_3 layer. These processes have potential to help prevent high O_3 transport down to the lower layers of the atmosphere and therefore help avoid AQ exeedances. Finally, this work shows the capabilities of LMOL for detecting SI and for helping the validation of GEOS-CF O_3 products.

Acknowledgements

LMOL, part of the TOLNET project is funded by the NASA Tropospheric Composition Program. G. Gronoff, T. Berkoff, L. Lei, W. Carrion are funded by LMOL. K.E. Knowland is supported by the NASA Modeling, Analysis and Prediction (MAP) program M. Shook is funded by the NASA Tropospheric Composition Program. A.O. Langford is supported by the NOAA Climate Program Office, Atmospheric Chemistry, Carbon Cycle, and Climate (AC4) Program. The MPLNET project is funded by the NASA Radiation Sciences Program and Earth Observing System. GEOS-CF is publicly available through OPenDAP and HTTP download (https://gmao.gsfc.nasa.gov/weather_prediction/GEOS-CF/data_access). The authors wish to thank the anonymous reviewers for their comments and suggestions.

LMOL data are publicly available on https://www-air.larc.nasa.gov/missions/TOLNet/

References

[1] M. A. Shapiro, Turbulent Mixing within Tropopause Folds as a Mechanism for the Exchange of Chemical Constituents between the Stratosphere and Troposphere., Journal of Atmospheric Sciences 37 (5) (1980) 994–1004. doi:10.1175/1520-0469(1980)037<0994:TMWTFA>2.0.CO;2.

[2] M. A. Shapiro, T. Hampel, A. J. Krueger, The arctic tropopause fold, Monthly Weather Review 115 (2) (01 Feb. 1987) 444 – 454. doi:10.1175/1520-0493(1987)115<0444:TATF>2.0.CO;2.
URL https://journals.ametsoc.org/view/journals/mwre/115/2/1520-0493_1987_115_0444_tatf_2_0_co_2.xml

[3] E. V. Browell, E. F. Danielsen, S. Ismail, G. L. Gregory, S. M. Beck, Tropopause fold structure determined from airborne lidar and in situ measurements, Journal of Geophysical Research: Atmospheres 92 (D2) (1987) 2112–2120. doi:10.1029/JD092iD02p02112.
URL https://agupubs.onlinelibrary.wiley.com/doi/abs/10.1029/JD092iD02p02112

[4] A. O. Langford, J. Brioude, O. R. Cooper, C. J. Senff, R. J. Alvarez II, R. M. Hardesty, B. J. Johnson, S. J. Oltmans, Stratospheric influence on surface ozone in the los angeles area during late spring and early summer of 2010, Journal of Geophysical Research: Atmospheres 117 (D21). arXiv:https://agupubs.onlinelibrary.wiley.com/doi/pdf/10.1029/2011JD016766, doi:10.1029/2011JD016766.
URL https://agupubs.onlinelibrary.wiley.com/doi/abs/10.1029/2011JD016766

[5] K. E. Knowland, R. M. Doherty, K. I. Hodges, L. E. Ott, The influence of mid-latitude cyclones on european background surface ozone, Atmospheric Chemistry and Physics 17 (20) (2017) 12421–12447. doi:10.5194/acp-17-12421-2017.
URL https://www.atmos-chem-phys.net/17/12421/2017/

[6] J. Dreessen, A sea level stratospheric ozone intrusion event induced within a thunderstorm gust front, Bulletin of the American Meteorological Society 100 (7) (2019) 1259–1275. arXiv:https://doi.org/10.1175/BAMS-D-18-0113.1, doi:10.1175/BAMS-D-18-0113.1.
URL https://doi.org/10.1175/BAMS-D-18-0113.1

[7] Q. Tang, M. J. Prather, Correlating tropospheric column ozone with tropopause folds: the Aura-OMI satellite data, Atmospheric Chemistry & Physics 10 (19) (2010) 9681–9688. doi:10.5194/acp-10-9681-2010.

[8] A. O. Langford, Stratosphere-troposphere exchange at the subtropical jet: Contribution to the tropospheric ozone budget at midlatitudes, Geo. Res. Let. 26 (16) (1999) 2449–2452. doi:10.1029/1999GL900556.

[9] W. B. Johnson, W. Viezee, Stratospheric ozone in the lower troposphere – i. presentation and interpretation of aircraft measurements, Atmospheric Environment (1967) 15 (7) (1981) 1309–1323.

[10] M. L. Büker, M. H. Hitchman, G. J. Tripoli, R. B. Pierce, E. V. Browell, M. A. Avery, Resolution dependence of cross-tropopause ozone transport over east Asia, J. Geophys. Res. 110 (D3), D03107. doi:10.1029/2004JD004739.
URL http://dx.doi.org/10.1029/2004JD004739

[11] M. Lin, A. M. Fiore, O. R. Cooper, L. W. Horowitz, A. O. Langford, H. Levy, B. J. Johnson, V. Naik, S. J. Oltmans, C. J. Senff, Springtime high surface ozone events over the western United States: Quantifying the role of stratospheric intrusions, J. Geophys. Res. 117 (D21), d00V22. doi:10.1029/2012JD018151.

[12] L. E. Ott, B. N. Duncan, A. M. Thompson, G. Diskin, Z. Fasnacht, A. O. Langford, M. Lin, A. M. Molod, J. E. Nielsen, S. E. Pusede, K. Wargan, A. J. Weinheimer, Y. Yoshida, Frequency and impact of summertime stratospheric intrusions over maryland during discover-aq (2011): New evidence from nasa's geos-5 simulations,

Journal of Geophysical Research: Atmospheres 121 (7) (2016) 3687–3706. arXiv:https://agupubs.onlinelibrary.wiley.com/doi/pdf/10.1002/2015JD024052, doi:10.1002/2015JD024052.
URL https://agupubs.onlinelibrary.wiley.com/doi/abs/10.1002/2015JD024052

[13] K. E. Knowland, L. E. Ott, B. N. Duncan, K. Wargan, Stratospheric Intrusion-Influenced Ozone Air Quality Exceedances Investigated in the NASA MERRA-2 Reanalysis, Geophysical Research Letters 44 (20) (2017) 10,691–10,701. doi:10.1002/2017GL074532.
URL https://agupubs.onlinelibrary.wiley.com/doi/full/10.1002/2017GL074532

[14] W. Woiwode, A. Dörnbrack, M. Bramberger, F. Friedl-Vallon, F. Haenel, M. Höpfner, S. Johansson, E. Kretschmer, I. Krisch, T. Latzko, H. Oelhaf, J. Orphal, P. Preusse, B.-M. Sinnhuber, J. Ungermann, Mesoscale fine structure of a tropopause fold over mountains, Atmospheric Chemistry & Physics 18 (21) (2018) 15643–15667. doi:10.5194/acp-18-15643-2018.

[15] M. Sprenger, H. Wernli, A northern hemispheric climatology of cross-tropopause exchange for the era15 time period (1979–1993), Journal of Geophysical Research: Atmospheres 108 (D12). arXiv:https://agupubs.onlinelibrary.wiley.com/doi/pdf/10.1029/2002JD002636, doi:https://doi.org/10.1029/2002JD002636.
URL https://agupubs.onlinelibrary.wiley.com/doi/abs/10.1029/2002JD002636

[16] EPA, National ambient air quality standards for o_3: Proposed decision, Federal Register 61 (241) (1997) 65717–65750.

[17] A. O. Langford, K. C. Aikin, C. S. Eubank, E. J. Williams, Stratospheric contribution to high surface ozone in Colorado during springtime, Geophysical Research Letters 36 (12) (2009) L12801. doi:10.1029/2009GL038367.

[18] A. O. Langford, R. J. Alvarez, J. Brioude, S. Evan, L. T. Iraci, G. Kirgis, S. Kuang, T. Leblanc, M. J. Newchurch, R. B. Pierce, C. J. Senff, E. L. Yates, Coordinated profiling of stratospheric intrusions and transported pollution by the Tropospheric Ozone Lidar Network (TOLNet) and NASA Alpha Jet experiment (AJAX): Observations and comparison to HYSPLIT, RAQMS, and FLEXPART, Atmospheric Environment 174 (2018) 1–14. doi:10.1016/j.atmosenv.2017.11.031.

[19] J. Robinson, A. Kotsakis, F. Santos, R. Swap, K. Knowland, G. Labow, V. Connors, M. Tzortziou, N. Abuhassan, M. Tiefengraber, A. Cede, Using networked pandora observations to capture spatiotemporal changes in total column ozone associated with stratosphere-to-troposphere transport, Atmospheric Research (2020) 104872doi:https://doi.org/10.1016/j.atmosres.2020.104872.
URL http://www.sciencedirect.com/science/article/pii/S0169809519308920

[20] H. Flentje, A. DöRnbrack, G. Ehret, A. Fix, C. Kiemle, G. Poberaj, M. Wirth, Water vapor heterogeneity related to tropopause folds over the North Atlantic revealed by airborne water vapor differential absorption lidar, Journal of Geophysical Research (Atmospheres) 110 (D3) (2005) D03115. doi:10.1029/2004JD004957.

[21] J. Ungermann, L. L. Pan, C. Kalicinsky, F. Olschewski, P. Knieling, J. Blank, K. Weigel, T. Guggenmoser, F. Stroh, L. Hoffmann, M. Riese, Filamentary structure in chemical tracer distributions near the subtropical jet following a wave breaking event, Atmospheric Chemistry & Physics 13 (20) (2013) 10517–10534. doi:10.5194/acp-13-10517-2013.

[22] P. S. Monks, A review of the observations and origins of the spring ozone maximum, Atmospheric Environment 34 (21) (2000) 3545 – 3561. doi:https://doi.org/10.1016/S1352-2310(00)00129-1.

URL http://www.sciencedirect.com/science/article/pii/S1352231000001291

[23] R. De Young, W. Carrion, R. Ganoe, D. Pliutau, G. Gronoff, T. Berkoff, S. Kuang, Langley mobile ozone lidar: ozone and aerosol atmospheric profiling for air quality research, Applied optics 56 (3) (2017) 721–730.

[24] T. Berkoff, G. Gronoff, J. Sparrow, L. A. Rodio, M. E. Buzanowicz, W. Carrion, Coastal and Over-Water Ozone Profile Observations Obtained by the NASA Langley Mobile Ozone Lidar System, in: AGU Fall Meeting Abstracts, Vol. 2018, 2018, pp. A51N–2386.

[25] J. T. Sullivan, T. Berkoff, G. Gronoff, T. Knepp, M. Pippin, D. Allen, L. Twigg, R. Swap, M. Tzortziou, A. M. Thompson, R. M. Stauffer, G. M. Wolfe, J. Flynn, S. E. Pusede, L. M. Judd, W. Moore, B. D. Baker, J. Al-Saadi, T. J. McGee, The Ozone Water-Land Environmental Transition Study: An Innovative Strategy for Understanding Chesapeake Bay Pollution Events, Bulletin of the American Meteorological Society 100 (2) (2019) 291–306. doi:10.1175/BAMS-D-18-0025.1.

[26] N. Dacic, J. T. Sullivan, K. E. Knowland, G. M. Wolfe, L. D. Oman, T. A. Berkoff, G. P. Gronoff, Evaluation of NASA's high-resolution global composition simulations: Understanding a pollution event in the Chesapeake Bay during the summer 2017 OWLETS campaign, Atmospheric Environment 222 (2020) 117133. doi:10.1016/j.atmosenv.2019.117133.

[27] T. Leblanc, M. A. Brewer, P. S. Wang, M. J. Granados-Muñoz, K. B. Strawbridge, M. Travis, B. Firanski, J. T. Sullivan, T. J. McGee, G. K. Sumnicht, L. W. Twigg, T. A. Berkoff, W. Carrion, G. Gronoff, A. Aknan, G. Chen, R. J. Alvarez, A. O. Langford, C. J. Senff, G. Kirgis, M. S. Johnson, S. Kuang, M. J. Newchurch, Validation of the TOLNet lidars: the Southern California Ozone Observation Project (SCOOP), Atmospheric Measurement Techniques 11 (11) (2018) 6137–6162. doi:10.5194/amt-11-6137-2018.

[28] G. Gronoff, J. Robinson, T. Berkoff, R. Swap, B. Farris, J. Schroeder, H. S. Halliday, T. Knepp, E. Spinei, W. Carrion, et al., A method for quantifying near range point source induced o3 titration events using co-located lidar and pandora measurements, Atmospheric environment 204 (2019) 43–52.

[29] B. M. Farris, G. P. Gronoff, W. Carrion, T. Knepp, M. Pippin, T. A. Berkoff, Demonstration of an off-axis parabolic receiver for near-range retrieval of lidar ozone profiles, Atmospheric Measurement Techniques 12 (1) (2019) 363–370.

[30] T. Leblanc, R. J. Sica, J. A. E. van Gijsel, S. Godin-Beekmann, A. Haefele, T. Trickl, G. Payen, F. Gabarrot, Proposed standardized definitions for vertical resolution and uncertainty in the NDACC lidar ozone and temperature algorithms - Part 1: Vertical resolution, Atmospheric Measurement Techniques 9 (8) (2016) 4029–4049. doi:10.5194/amt-9-4029-2016.

[31] T. Leblanc, R. J. Sica, J. A. E. van Gijsel, S. Godin-Beekmann, A. Haefele, T. Trickl, G. Payen, G. Liberti, Proposed standardized definitions for vertical resolution and uncertainty in the NDACC lidar ozone and temperature algorithms - Part 2: Ozone DIAL uncertainty budget, Atmospheric Measurement Techniques 9 (8) (2016) 4051–4078. doi:10.5194/amt-9-4051-2016.

[32] E. J. Welton, J. R. Campbell, J. D. Spinhirne, I. Scott, V. Stanley, Global monitoring of clouds and aerosols using a network of micropulse lidar systems, Vol. 4153 of Society of Photo-Optical Instrumentation Engineers (SPIE) Conference Series, 2001, pp. 151–158. doi:10.1117/12.417040.

[33] J. R. Lewis, J. R. Campbell, S. A. Stewart, I. Tan, E. J. Welton, S. Lolli, Determining cloud thermodynamic phase from the polarized micro pulse lidar, Atmospheric Measurement Techniques 13 (12) (2020) 6901–6913. doi:10.5194/amt-13-6901-2020.
URL https://amt.copernicus.org/articles/13/6901/2020/

[34] C. J. Flynn, A. Mendoza, Y. Zheng, S. Mathur, Novel polarization-sensitive micropulse lidar measurement technique, Optics Express 15 (6) (2007) 2785–2790. doi:10.1364/OE.15.002785.

[35] L. Zhang, M. Lin, A. O. Langford, L. W. Horowitz, C. J. Senff, E. Klovenski, Y. Wang, I. Alvarez, Raul J., I. Petropavlovskikh, P. Cullis, C. W. Sterling, J. Peischl, T. B. Ryerson, S. S. Brown, Z. C. J. Decker, G. Kirgis, S. Conley, Characterizing sources of high surface ozone events in the southwestern US with intensive field measurements and two global models, Atmospheric Chemistry & Physics 20 (17) (2020) 10379–10400. doi:10.5194/acp-20-10379-2020.

[36] C. A. Keller, K. E. Knowland, B. N. Duncan, J. Liu, D. C. Anderson, S. Das, R. A. Lucchesi, E. W. Lundgren, J. M. Nicely, E. Nielsen, L. E. Ott, E. Saunders, S. A. Strode, P. A. Wales, D. J. Jacob, S. Pawson, Description of the nasa geos composition forecast modeling system geos-cf v1.0, Journal of Advances in Modeling Earth Systems 13 (4) (2021) e2020MS002413, e2020MS002413 2020MS002413. arXiv:https://agupubs.onlinelibrary.wiley.com/doi/pdf/10.1029/2020MS002413, doi:https://doi.org/10.1029/2020MS002413.
URL https://agupubs.onlinelibrary.wiley.com/doi/abs/10.1029/2020MS002413

[37] C. Orbe, D. W. Waugh, H. Yang, J.-F. Lamarque, S. Tilmes, D. E. Kinnison, Tropospheric transport differences between models using the same large-scale meteorological fields, Geo. Res. Lett. 44 (2) (2017) 1068–1078. doi:10.1002/2016GL071339.

[38] R. Lucchesi, File specification for geos-5 fp-it (forward processing for instrument teams), GMAO Office Note No. 2 (Version 1.4) 58pp,available from http://gmao.gsfc.nasa.gov/pubs/office_notes.php.

[39] I. Bey, D. J. Jacob, R. M. Yantosca, J. A. Logan, B. D. Field, A. M. Fiore, Q. Li, H. Y. Liu, L. J. Mickley, M. G. Schultz, Global modeling of

tropospheric chemistry with assimilated meteorology: Model description and evaluation, J. Geo. Res. 106 (D19) (2001) 23,073–23,095. doi:10.1029/2001JD000807.

[40] C. A. Keller, M. S. Long, R. M. Yantosca, A. M. Da Silva, S. Pawson, D. J. Jacob, HEMCO v1.0: a versatile, ESMF-compliant component for calculating emissions in atmospheric models, Geoscientific Model Development 7 (4) (2014) 1409–1417. doi:10.5194/gmd-7-1409-2014.

[41] M. S. Long, R. Yantosca, J. E. Nielsen, C. A. Keller, A. da Silva, M. P. Sulprizio, S. Pawson, D. J. Jacob, Development of a grid-independent GEOS-chem chemical transport model as an atmospheric chemistry module for Earth System Models, Geoscientific Model Development Discussions 7 (6) (2014) 7505–7524. doi:10.5194/gmdd-7-7505-2014.

[42] L. Hu, C. A. Keller, M. S. Long, T. Sherwen, B. Auer, A. Da Silva, J. E. Nielsen, S. Pawson, M. A. Thompson, A. L. Trayanov, K. R. Travis, S. K. Grange, M. J. Evans, D. J. Jacob, Global simulation of tropospheric chemistry at 12.5 km resolution: performance and evaluation of the geos-chem chemical module (v10-1) within the nasa geos earth system model (geos-5 esm), Geoscientific Model Development 11 (11) (2018) 4603–4620. doi:10.5194/gmd-11-4603-2018.
URL https://gmd.copernicus.org/articles/11/4603/2018/

[43] S. D. Eastham, D. K. Weisenstein, S. R. Barrett, Development and evaluation of the unified tropospheric–stratospheric chemistry extension (ucx) for the global chemistry-transport model geos-chem, Atmospheric Environment 89 (2014) 52–63.

[44] J. R. Ziemke, M. A. Olsen, J. C. Witte, A. R. Douglass, S. E. Strahan, K. Wargan, X. Liu, M. R. Schoeberl, K. Yang, T. B. Kaplan, S. Pawson, B. N. Duncan, P. A. Newman, P. K. Bhartia, M. K. Heney, Assessment and applications of nasa ozone data products derived from aura omi/mls satellite measurements in context of the gmi chemical

transport model, Journal of Geophysical Research: Atmospheres 119 (9) (2014) 5671–5699. arXiv:https://agupubs.onlinelibrary.wiley.com/doi/pdf/10.1002/2013JD020914, doi:10.1002/2013JD020914.
URL https://agupubs.onlinelibrary.wiley.com/doi/abs/10.1002/2013JD020914

[45] L. Flynn, C. Long, X. Wu, R. Evans, C. T. Beck, I. Petropavlovskikh, G. McConville, W. Yu, Z. Zhang, J. Niu, E. Beach, Y. Hao, C. Pan, B. Sen, M. Novicki, S. Zhou, C. Seftor, Performance of the ozone mapping and profiler suite (omps) products, Journal of Geophysical Research: Atmospheres 119 (10) (2014) 6181–6195. arXiv:https://agupubs.onlinelibrary.wiley.com/doi/pdf/10.1002/2013JD020467, doi:10.1002/2013JD020467.
URL https://agupubs.onlinelibrary.wiley.com/doi/abs/10.1002/2013JD020467

[46] K. E. Knowland, File specification for geos-cf products. nasa ntrs, available at https://ntrs.nasa.gov/search.jsp?r=20190031877.

[47] E. V. Browell, S. T. Shipley, S. Ismail, Ultraviolet DIAL measurements of O_3 profiles in regions of spatially inhomogeneous aerosols, Applied Optics 24 (17) (1985) 2827–2836. doi:10.1364/AO.24.002827.

[48] A. O. Langford, C. D. Masters, M. H. Proffitt, E.-Y. Hsie, A. F. Tuck, Ozone measurements in a tropopause fold associated with a cut-off low system, Geophysical Research Letters 23 (18) (1996) 2501–2504. arXiv:https://agupubs.onlinelibrary.wiley.com/doi/pdf/10.1029/96GL02227, doi:10.1029/96GL02227.
URL https://agupubs.onlinelibrary.wiley.com/doi/abs/10.1029/96GL02227

[49] A. O. Langford, C. D. Masters, M. H. Proffitt, E. Y. Hsie, A. F. Tuck, Correction to "ozone measurements in a tropopause fold associated with

a cut-off low system", Geophysical Research Letters 24 (1) (1997) 109–109. arXiv:https://agupubs.onlinelibrary.wiley.com/doi/pdf/10.1029/96GL03795, doi:10.1029/96GL03795.
URL https://agupubs.onlinelibrary.wiley.com/doi/abs/10.1029/96GL03795

[50] A. Stohl, P. Bonasoni, P. Cristofanelli, W. Collins, J. Feichter, A. Frank, C. Forster, E. Gerasopoulos, H. Gäggeler, P. James, T. Kentarchos, H. Kromp-Kolb, B. Krüger, C. Land, J. Meloen, A. Papayannis, A. Priller, P. Seibert, M. Sprenger, G. J. Roelofs, H. E. Scheel, C. Schnabel, P. Siegmund, L. Tobler, T. Trickl, H. Wernli, V. Wirth, P. Zanis, C. Zerefos, Stratosphere-troposphere exchange: A review, and what we have learned from staccato, Journal of Geophysical Research: Atmospheres 108 (D12). arXiv:https://agupubs.onlinelibrary.wiley.com/doi/pdf/10.1029/2002JD002490, doi:10.1029/2002JD002490.
URL https://agupubs.onlinelibrary.wiley.com/doi/abs/10.1029/2002JD002490

[51] M. D. Guasta, M. Morandi, L. Stefanutti, S. Balestri, E. Kyro, M. Rummukainen, R. Kivi, V. Rizi, B. Stein, C. Wedekind, B. Mielke, R. Matthey, V. Mitev, M. Douard, Lidar observation of spherical particles in a -65degree cold cirrus observed above Sodankyla (Finland) during S.E.S.A.M.E., Journal of Aerosol Science 29 (3) (1998) 357–374. doi:10.1016/S0021-8502(97)10008-8.

[52] F. Khosrawi, R. Müller, J. Beuermann, P. Konopka, C. Schiller, Dehydration in the northern hemisphere mid-latitude tropopause region observed during STREAM 1998, Tellus Series B Chemical and Physical Meteorology B 58 (3) (2006) 206–217. doi:10.1111/j.1600-0889.2006.00182.x.

[53] J. Reichardt, A. Ansmann, M. Serwazi, C. Weitkamp, W. Michaelis, Unexpectedly low ozone concentration in midlatitude tropospheric ice clouds:

A case study, Geo. Res. Let. 23 (15) (1996) 1929–1932. doi:10.1029/96GL01856.

[54] S. Roumeau, P. Brémaud, E. Rivière, S. Baldy, J. L. Baray, Tropical cirrus clouds: A possible sink for ozone, Geophysical Research Letters 27 (15) (2000) 2233–2236. doi:10.1029/1999GL010898.

[55] S. Borrmann, S. Solomon, J. E. Dye, B. Luo, The potential of cirrus clouds for heterogeneous chlorine activation, Geo. Res. Let. 23 (16) (1996) 2133–2136. doi:10.1029/96GL01957.

[56] M. P. Chipperfield, S. Dhomse, R. Hossaini, W. Feng, M. L. Santee, M. Weber, J. P. Burrows, J. D. Wild, D. Loyola, M. Coldewey-Egbers, On the cause of recent variations in lower stratospheric ozone, Geophysical Research Letters 45 (11) (2018) 5718–5726. arXiv:https://agupubs.onlinelibrary.wiley.com/doi/pdf/10.1029/2018GL078071, doi:https://doi.org/10.1029/2018GL078071.
URL https://agupubs.onlinelibrary.wiley.com/doi/abs/10.1029/2018GL078071

[57] A. Meier, J. Hendricks, Model studies on the sensitivity of upper tropospheric chemistry to heterogeneous uptake of HNO3 on cirrus ice particles, Journal of Geophysical Research: Atmospheres 107 (D23) (2002) ACH 9–1–ACH 9–16, _eprint: https://agupubs.onlinelibrary.wiley.com/doi/pdf/10.1029/2001JD000735.
doi:https://doi.org/10.1029/2001JD000735.
URL https://agupubs.onlinelibrary.wiley.com/doi/abs/10.1029/2001JD000735

[58] D. J. Jacob, Heterogeneous chemistry and tropospheric ozone, Atmospheric Environment 34 (12) (2000) 2131–2159. doi:10.1016/S1352-2310(99)00462-8.
URL http://www.sciencedirect.com/science/article/pii/S1352231099004628

[59] Z. Wang, K. Sassen, Ozone Destruction in Continental Stratus Clouds: An Aircraft Case Study, JOURNAL OF APPLIED METEOROLOGY 39 (2000) 12.

[60] M. Y. Arshinov, B. D. Belan, G. N. Tolmachev, A. V. Fofonov, The scale of ozone destruction in clouds, Atmospheric and Oceanic Optics 23 (2) (2010) 106–110. doi:10.1134/S1024856010020041.
URL https://doi.org/10.1134/S1024856010020041

[61] J. R. Campbell, E. J. Welton, N. A. Krotkov, K. Yang, S. A. Stewart, M. D. Fromm, Likely seeding of cirrus clouds by stratospheric Kasatochi volcanic aerosol particles near a mid-latitude tropopause fold, Atmospheric Environment 46 (2012) 441–448. doi:10.1016/j.atmosenv.2011.09.027.

[62] K. Sassen, D. O'C. Starr, G. G. Mace, M. R. Poellot, S. H. Melfi, W. L. Eberhard, J. D. Spinhirne, E. W. Eloranta, D. E. Hagen, J. Hallett, The 5-6 December 1991 FIRE IFO II Jet Stream Cirrus Case Study: Possible Influences of Volcanic Aerosols., Journal of Atmospheric Sciences 52 (1) (1995) 97–123. doi:10.1175/1520-0469(1995)052<0097:TDFIIJ>2.0.CO;2.